

# Superheterodyne Rydberg S-band receiver with a multi-tone local oscillator based on an atomic transition loop

JAN NOWOSIELSKI,<sup>1,2</sup> MATEUSZ MAZELANIK,<sup>1</sup> WOJCIECH WASILEWSKI,<sup>1,2</sup> AND MICHAŁ PARNIAK<sup>1,2,\*</sup>

<sup>1</sup>*Centre for Quantum Optical Technologies, Centre of New Technologies, University of Warsaw, S. Banacha 2c, 02-097 Warsaw, Poland*

<sup>2</sup>*Faculty of Physics, University of Warsaw, L. Pasteura 5, 02-093 Warsaw, Poland*

\*[mparniak@fuw.edu.pl](mailto:mparniak@fuw.edu.pl)

**Abstract:** Atomic-vapor sensors based on Rydberg atoms now face a transition towards practical applications, with several outstanding challenges. To achieve the best sensitivities, a superheterodyne mode of operation is desired, which requires the presence of a local oscillator in the vapor cell. This local oscillator hinders several advantages of the sensor, such as stealthy and all-optical operation. We propose and realize a detection scheme, which avoids some of those problems by using multi-tone mixing, where direct usage of the local oscillator at the same frequency is not required. Our scheme is further elaborated on using efficient theoretical methods to predict the performance of the sensor. Our sensor operates at the S-band frequency, known for its usage in IEEE 802.11 (Wi-Fi) networks, without interfering with the signal itself.

## 1. Introduction

Rydberg atom-based electromagnetic (EM) radiation sensors are a promising technology already holding a solid position in the scientific community. The technology utilises large transition dipole moments between Rydberg states to achieve EM field sensitivity on par with specialized electronics [1, 2]. Yet, it still allows for high detection bandwidth [3, 4] and offers advantages such as extraordinary tunability and, importantly, self calibration feature based on fundamental constants. These naturally arose features combined with the possibility of relatively low complexity of the sensors and the possibility of miniaturization and packaging [5–7] drove the attention of the engineering community that joined the effort of maturing the technology. As technology matures, new scientific and practical applications are born.

The established detection schemes allow measuring the RF EM field amplitude [8, 9], detecting frequency and amplitude modulation [10, 11], phase-sensitive measurement [12–14] and photon counting via RF-to-optical conversion [15–17]. Moreover, the properties of Rydberg atoms allow for measurement of different properties of oncoming EM field such as angle of arrival [18], and polarization [19, 20]. Apart from applications in electrometry, in recent years, multiple groups have presented communication schemes employing phase-sensitive Rydberg-based receivers [21, 22].

The first sensors to be field-deployed are most likely the simplest ones. The lowest complexity, amplitude sensor based on Autler-Townes (AT) effect spectroscopy, while having limited sensitivity enables self-referencing by linking the measured amplitude with the Rabi frequency and thus dipole moment. However, in many applications higher sensitivity and phase-resolving detection are desired. This is offered by the superheterodyne sensor that employs an additional field acting as a local oscillator which as in the case of standard phase-sensitive detection of the electronic signal needs to be close in frequency and stronger than the signal itself. Thus, the additional field can disturb the source of the measured field and is often generally undesired. Interestingly enough, phase-sensitive detection can be achieved without employing a local oscillator utilizing the loop energy schemes. The phase-sensitivity of such setups has been

described theoretically [23–25], and in recent years, multiple groups have utilized it to perform the phase-sensitive detection in case of all-optical [26] and microwave-optical [26–28] schemes. An interesting case arises when considering a fully microwave loop, which up to this moment was proposed only theoretically [29], as a phase between generated microwave fields can be easily controlled electronically. In this paper, we propose an experimental implementation of such setup consisting of three different microwave fields, and compare measured phase-dependent probe transmission spectra as fields to the numerical predictions. Additionally, we characterize our setup as a receiver, finding its sensitivity and response range.

## 2. Experimental setup

### 2.1. Energy level scheme

In the experiment, we consider a 6-level energy ladder of  $^{85}\text{Rb}$  depicted in the Fig 1a. In the following setup, the probe laser is tuned to the  $D_2$  transition between ground state  $5^2S_{1/2}(F = 3)$  and  $5^2P_{3/2}(F = 4)$ . The second 776 nm and third 1268 nm fields coupled to the  $5^2P_{3/2}(F = 4) \rightarrow 5^2D_{5/2}(F = 5)$  and  $5^2D_{5/2}(F = 5) \rightarrow 32^2F_{7/2}$  transitions respectively excite atoms to the Rydberg state. The overlapping electromagnetically induced transparency effects (EIT) [30] caused by both fields lead to the emergence of the so-called electromagnetically induced absorption effect (EIA) [31].

Next field, coupled to the  $32^2F_{7/2} \rightarrow 32^2G_{9/2}$  transition with the frequency, we call the signal (SIG) microwave (MW) field with the frequency  $f_{\text{SIG}} \approx 2.5$  GHz. To perform the phase-sensitive measurement of the SIG field we utilize the all-microwave loop interferometry scheme with two additional MW fields. The dressing (DRS) field with the frequency  $f_{\text{DRS}} \approx 500$  MHz excites atoms through the  $32^2G_{9/2} \rightarrow 32^2H_{11/2}$  transition and the loop is then closed by the coupling (CPL) field at the frequency  $f_{\text{CPL}} \approx 1.5$  GHz, which drives atoms from the  $32^2F_{7/2}$  to the  $32^2H_{11/2}$  via the two-photon transition.

It was shown in other works that in the case of the resonance of all the fields in the loop, i.e.  $f_{\text{SIG}} + f_{\text{DRS}} - 2f_{\text{CPL}} = 0$  the probe transmission through the atomic medium depends solely on the phase between fields. In the non-resonant case, that is if one of the fields is detuned from the loop resonance, the phase between fields becomes time-dependent and is equal  $\varphi = 2\pi \cdot f_{\text{OPT}}t$ , where  $t$  is time and  $f_{\text{OPT}} = f_{\text{SIG}} + f_{\text{DRS}} - 2f_{\text{CPL}}$  is the frequency mismatch, which can be interpreted as the frequency of the optical (OPT) signal. Moreover, if the SIG was phase-modulated, the modulation could be then recovered by measuring the transmission via the photodiode (PD) and then demodulating measured PD signal at the beat note frequency.

### 2.2. Experimental setup

Our experimental setup is built around room-temperature ( $22.5^\circ\text{C}$ )  $^{85}\text{Rb}$  atoms, and its simplified scheme is depicted in Fig 1b. To partially reduce the thermal (Doppler) broadening the pair of 776 and 1268 nm beams and the probe beam counter-propagate in the cell. All beams are circularly polarized, with the probe beam being left-handed circularly polarized, and coupling beams being right-handed circularly polarized. All beams focused inside the cylindrical vapor cell with a length equal to 58 mm. The powers of lasers are chosen to maximize the EIA effect, which is achieved for probe laser power equal to  $P_{780} = 1.5 \mu\text{W}$ , and powers of 776 and 1268 nm lasers equal to  $P_{776} = 2.4$  mW and  $P_{1268} = 85$  mW and all laser beam waists equal to  $w = 300 \mu\text{m}$ . All lasers are frequency-stabilized to the master laser via the cavity setups.

The MW signals are generated using the LMX2595EVM frequency synthesizers. The SIG field is generated by sending a signal at the frequency  $f_{\text{SIG}} = 2514$  MHz via the controllable attenuator to the commercially available Wi-Fi antenna. The CPL and DRS fields are generated by two additional frequency synthesizers at the frequencies  $f_{\text{DRS}} = 510.4$  MHz and  $f_{\text{CPL}} = 1512.2$  MHz. The signals are then combined via the frequency splitter and sent to the capacitor-like antenna

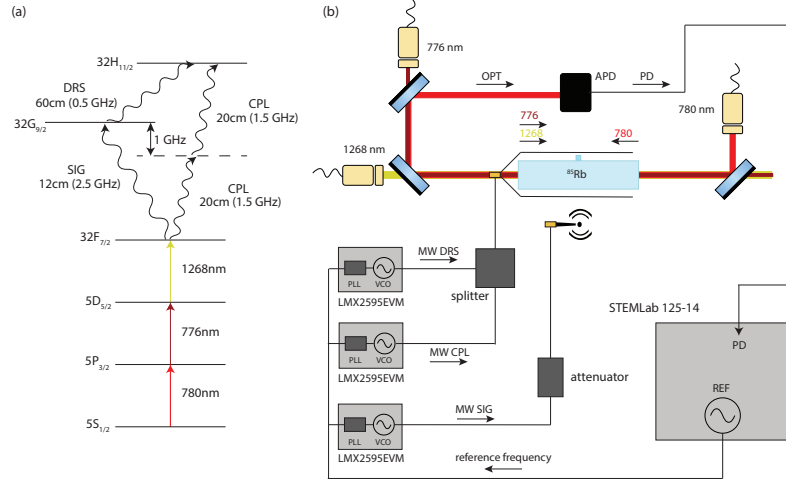


Fig. 1. (a)  $^{85}\text{Rb}$  energy level configuration used in the experiment. (b) scheme of the used experimental setup. MW - microwave, SIG - signal, CPL - coupling, DRS - dressing, APD - avalanche photodiode, OPT - optical signal, PD - photodiode signal, PLL - phase-locked loop, VCO - voltage-controlled oscillator.

mounted around the rubidium cell. The frequencies of the MW fields are chosen to optimize the atomic response. To have a stable and controllable phase between the MW fields all the frequency synthesizers get the same reference frequency from the STEMLab 125-14 multipurpose tool.

To perform the phase-sensitive detection, used to calibrate the receiver, as well as measure atomic response range, the 776 and 1268 nm lasers are tuned to their respective transitions and the probe laser is detuned by 3 MHz to the lower frequencies in order to maximize the atomic response to the MW fields. The probe transmission is measured by the avalanche photodiode with the 50 MHz bandwidth and the measured PD signal is sent to the STEMLab 125-14 multipurpose tool for further processing. Powers of the CPL and DRS fields for the measurements of sensitivity and atomic response range are also optimized to maximize the atomic response and the Rabi frequencies for both transitions are equal to  $\Omega_{\text{DRS}} = 2\pi \cdot 10.1 \text{ MHz}$  and  $\Omega_{\text{CPL}} = 2\pi \cdot 7.5 \text{ MHz}$ . It is important to note that the mentioned  $\Omega_{\text{CPL}}$  refers to the effective Rabi frequency of the two-photon transition.

### 3. Results

#### 3.1. Comparison with theoretical predictions

As mentioned in a previous section, the loop scheme consisting only of the MW fields allows for full control and prediction of the phase between the fields. Due to that reason, it is possible to fit the theoretical model predicting the behaviour of the probe transmission as a function of phase between MW fields to the experimental data. The experimental data was gathered for the case, where the EIT caused by 1268 nm laser was detuned by about 30 MHz to the lower probe frequencies, so the EIT caused by 776 nm and 1268 nm lasers do not overlap. Moreover in order to get better fits of the transmission spectra the SIG and DRS were detuned by  $\Delta = -5 \text{ MHz}$ . The measurements are performed by measuring the probe transmission with a locked probe laser, which after each measurement is relocked at the frequency detuned by  $\Delta f$  from the previous

one and the probe transmission is measured again. The sequence is then repeated over the probe frequency range, where the EIT caused by 1268 nm laser is visible.

As the impact of the SIG and DRS could be directly seen in the probe transmission spectrum, the Rabi frequencies of both those fields were found beforehand by fitting the transmission spectra to the steady state solution of the Lindblad equation for this path of the energy level loop. The effective Rabi frequency of the two-photon transition induced by the CPL was then found by fitting the solution of the Lindblad equation to the resonant case of the closed loop with all the MW fields turned on, using recently proposed numerical and theoretical framework [32]. For computational simplicity, the two-photon transition was assumed to be a single transition between two states. Thus, the Rabi frequency of the CPL field is the effective Rabi frequency of the two-photon transition. Using found values we performed the calculations for the time-dependent case. We compare the theoretical predictions with the experimental data in two situations: one called weak field regime, where the Stark shift of the overlapping Rydberg states due to the MW fields is negligible, and one in the strong field regime, where it becomes prominent and impacts the quality of the fit.

Both measurements were performed for the beat note frequency equal to  $f_{\text{OPT}} = 1.9$  kHz. In the case of the weak field regime, the Rabi frequencies of the MW fields were equal to  $\Omega_{\text{SIG}} = 2\pi \cdot 10.5$  MHz,  $\Omega_{\text{DRS}} = 2\pi \cdot 7.8$  MHz and  $\Omega_{\text{CPL}} = 2\pi \cdot 0.5$  MHz. The comparison between the experimental data and the theoretical predictions is shown in Fig 2. The 2D maps in the upper row represent the probe transmission as a function of the phase between MW fields and the probe detuning for the experimental data (left) and simulations (right). The dashed lines on both maps represent the cross-sections shown in the lower row. It can be seen that in the weak fields regime the theoretical prediction fits experimental data properly and the behaviour of the probe transmission as the function of the loop phase can be predicted.

In the case of strong fields, the Rabi frequencies were found to be  $\Omega_{\text{SIG}} = 2\pi \cdot 14$  MHz,  $\Omega_{\text{DRS}} = 2\pi \cdot 10.1$  MHz and  $\Omega_{\text{CPL}} = 2\pi \cdot 1.8$  MHz. The comparison between the experimental data and numerical predictions is shown in Fig 3. The mismatch between theoretical predictions and experimental data can be seen, which becomes more prominent for the positive probe detunings. Such divergence from the numerical simulations can be attributed to the Stark shifts of the degenerate Rydberg states caused mostly by the single-photon effects caused by the CPL field.

### 3.2. Calibration of the microwave field

The whole calibration procedure uses similar methods as our previous work regarding MW field detection at this transitions [33]. To find the receiver's sensitivity and the noise level, the calibration of its response to the MW fields is required. For the calibration, we detune the 1268 nm laser by 25 MHz to the lower probe frequencies, so the EIT caused by the 1268 nm and 776 nm do not overlap with each other. We then measure the transmission spectrum with the EIT splitting caused by the SIG field. The measurement is performed for the highest power of the SIG field being  $-15$  dBm. To change the power of the SIG field we use the controllable attenuator precise up to  $\pm 0.5$  dBm and an additional 3 dBm and 10 dBm attenuators which were added between measurements to probe the full dynamic range of the receiver. For the absolute calibration, we measure the transmission spectra for the attenuations from 0 to 15 dB with the step of 3 dB. To perform the absolute calibration we then fit the numerical solutions for the steady state of the Lindblad equation to the experimental data, from which we find the Rabi frequencies of the SIG field as a function of the signal attenuation. Based on the found Rabi frequencies we calculate the amplitude of the electric field given as  $A = \frac{\hbar\Omega}{d}$ , where  $\Omega$  is the Rabi frequency and  $d$  is the dipole moment of the transition found using the Alkali Rydberg Calculator [34]. In the considered experimental setup, the dipole moment equals  $d = 384a_0e$ , where  $a_0$  is the Bohr radius and  $e$  is the electron charge. To find the absolute calibration line we then fit a line

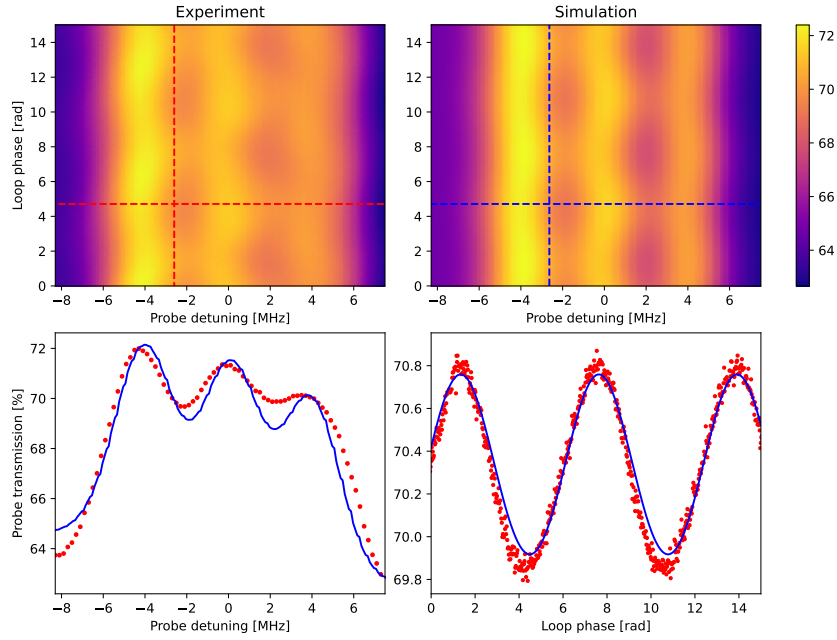


Fig. 2. Comparison between measured data and numerical predictions for the probe transmission spectrum as a function of the phase between MW fields in the weak-field case. The 2D maps in the upper row represent the probe transmission as a function of probe detuning and the phase for the experimental data and numerical predictions. The plots in the lower row represent cross-sections through the specific phase (left), and probe detuning (right), which was chosen to show the point with the strongest response to the MW fields.

function with a fixed slope equal to  $-1$  to the electric field amplitude as a function of the signal attenuation in the logarithmic scale thus acquiring the constant term of the calibration line.

In the case of the weaker SIG fields, absolute calibration is impossible due to their impact not being visible directly in the absorption spectrum. Because of that, the receiver's response needs to be measured differently and then calibrations in both regimes can be merged to acquire the relation between the electric field amplitude and the signal attenuation spanning the whole response range. To measure the response in that regime we utilize the phase-sensitive detection with the OPT signal frequency equal to  $f_{\text{OPT}} = 5$  MHz, for which we measure 100 subsequent waveforms of the Fourier power spectra of the PD signal over the 0.26 ms. We repeat that measurement for the SIG powers of  $-15$ ,  $-17$ ,  $-21$ ,  $-34$  dBm and signal attenuations from 0 dB to 30 dB with the step of 2 dB. Based on measured Fourier power spectra we then find the PD signal power level by taking the maximum value of the averaged Fourier power spectrum in the range of 1 MHz around the expected value of  $f_{\text{OPT}}$ . Additionally, the noise power level is found by similarly measuring the noise power spectra and then averaging it over the frequency range in which we looked for the PD signal power level.

For the calculated PD signal power level we consider the logarithmic scale, in which the power level changes linearly with the attenuation. For each SIG power, we fit the linear function with the slope value fixed to  $-1$ . Points for the highest signal power for the phase-sensitive detection are shifted to lie on the same line as points from the absolute calibration, allowing us to calculate the amplitude of the electric field based on the PD signal power level for the phase-sensitive detection. Fitted lines are then shifted to continue the absolute calibration line, spanning the whole range of

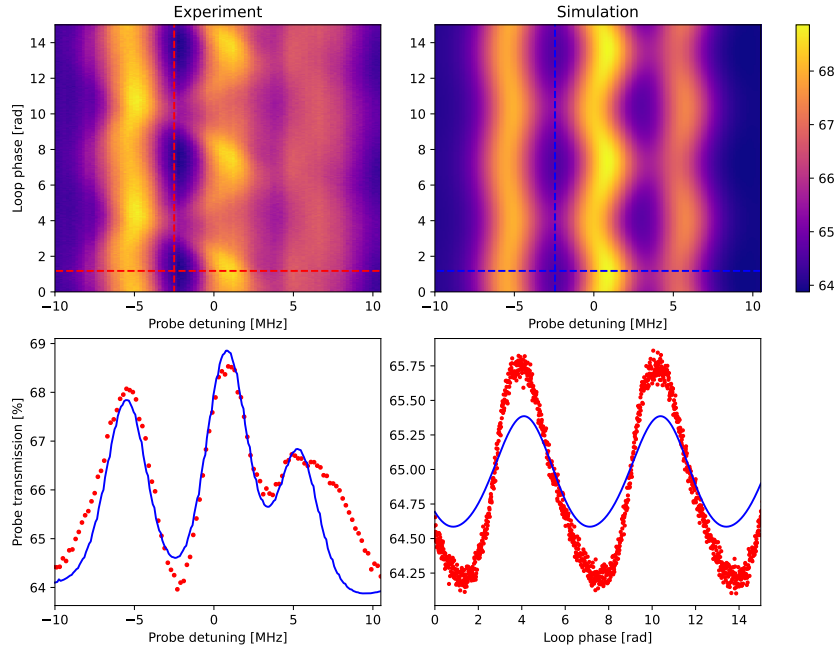


Fig. 3. Comparison between measured data and numerical predictions for the probe transmission spectrum as a function of the phase between MW fields in the strong-field case. The 2D maps in the upper row represent the probe transmission as a function of probe detuning and the phase for the experimental data and numerical predictions. The plots in the lower row represent cross-sections through the specific phase (left), and probe detuning (right), which was chosen to show the point with the strongest response to the MW fields.

the atomic response from saturation down to noise. Moreover shifting the calibration lines to extend the absolute calibration line gives us the relation between the amplitude of the electric field and the PD signal power level.

Using the found relation, we calculate the amplitude of the electric field for which the PD signal power level is equal to the noise power level, which was checked to be the shot-noise of the probe laser. The electric field amplitude corresponding to that signal level is equal to  $(200 \pm 20) \mu\text{V cm}^{-1}$  which in case of the 0.26 ms measurement time window translates to a noise level equal to  $(3.2 \pm 0.3) \mu\text{V cm}^{-1} \text{ Hz}^{-0.5}$ . The relation between the electric field amplitude and the PD signal attenuation together with the calibration line are shown in Fig 4. We also find the amplitude of the SIG field corresponding to the saturation level, which we define as a power level 1 dB weaker than the power for which the change in the atomic response due to changing signal attenuation becomes nonlinear. The calculated value of the amplitude of the electric field corresponding to the saturation level is equal to  $A_{sat} = (7.5 \pm 0.2) \text{ mV cm}^{-1}$ .

### 3.3. Atomic response range

To further characterize the receiver we measure the atomic response range in two distinct cases. In both cases the amplitude of the SIG field is constant and equal to  $A = (7.0 \pm 0.2) \text{ mV cm}^{-1}$ . In the first case, we only change the  $f_{\text{SIG}}$ , while keeping the rest of the MW fields at the constant frequencies, thus also changing the  $f_{\text{OPT}}$  in the process. To measure the atomic response at different frequencies we change the SIG frequency by 3 MHz in the range from 2480 MHz to 2540 MHz. For each SIG frequency we measure 100 waveforms of the Fourier power spectrum

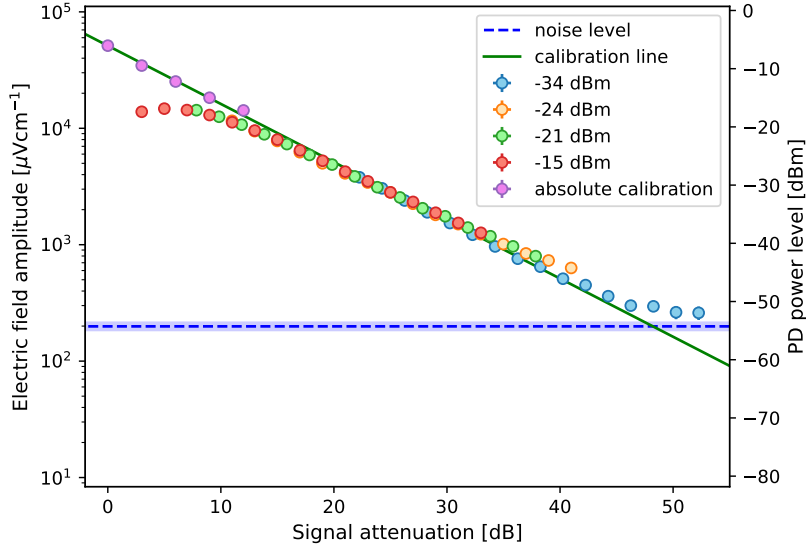


Fig. 4. Amplitude of the SIG field (left vertical axis) as the function of signal attenuation. The right vertical axis refers to the PD signal power level calculated from the Fourier power spectrum for phase-sensitive detection. The data points were gathered during the absolute calibration and phase-sensitive detection. The blue area around the shot noise level corresponds to the standard error of the calculated value.

of the PD signal with the measurement time of 0.26 ms. The PD power level is then found by taking the maximum value of the power spectrum in the range of 1 MHz around the expected value of  $f_{\text{OPT}}$ . Such measured atomic response as a function of the SIG field frequency can be seen in Fig 5 together with the shot-noise power level derived by averaging the noise power level over the whole spectrum and all the measurements. As it can be seen in Fig 5, the atomic response drops to the shot-noise level at the OPT signal frequencies of about  $f_{\text{OPT}} = \pm 20$  MHz, which translates to the  $f_{\text{SIG}} = 2534$  MHz and  $f_{\text{SIG}} = 2494$  MHz.

In the second case, we consider the frequency changes for both SIG and CPL fields in such a way, that the value of  $f_{\text{OPT}}$  remains fixed and equal to  $f_{\text{OPT}} = 5$  MHz. The measurements are performed by detuning both fields by frequencies in the range  $f \in [-145, 145]$  MHz with the step of 5 MHz. For each frequency, we measure the Fourier power spectrum with all the parameters being the same as in the previous case. For each of the detunement we gather 100 consecutive waveforms of the Fourier power spectrum of the PD signal with the measurement time of 0.26 ms. The signal's power level is found by taking the maximum value in the frequency range of 1 MHz around the expected beat note frequency of 5 MHz from the averaged Fourier power spectrum and its variance is found by taking the variance of the maximum value over each of the waveforms. The measured atomic response as a function of SIG field frequency together with the noise power level can be seen in Fig 6. As it can be seen from the figure, the atomic response drops to the near the shot-noise power level for the SIG frequencies of about  $f_{\text{SIG}} \approx 2450$  MHz and  $f_{\text{SIG}} \approx 2550$  MHz.

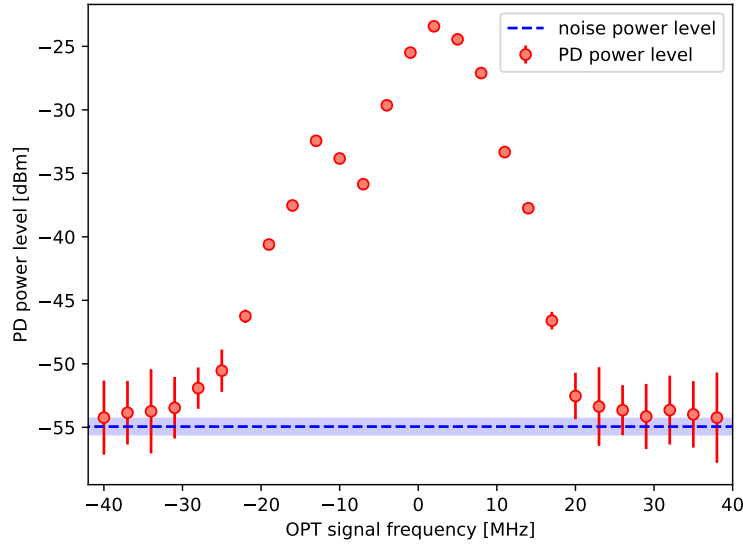


Fig. 5. Atomic response power level as a function of the frequency of the OPT signal together with the shot-noise power level. The atomic response was measured for different frequencies of the SIG field yielding different values of  $f_{\text{OPT}}$ . The blue area around the shot-noise power level corresponds to the standard error of the calculated value.

#### 4. Summary

In this paper, we presented the phase-sensitive detection scheme using 3 different MW fields, one of which drives atoms via the two-photon transition. Utilizing the phase-stability of the MW fields we compared measured phase-dependent transmission spectra to the theoretical predictions acquired from solving the time-dependent Lindblad equation. We characterized the receiver in terms of sensitivity achieving the value of  $(3.2 \pm 0.3) \mu\text{V cm}^{-1} \text{Hz}^{-0.5}$ , as well as its frequency response range. Similar behaviour of the Rydberg atom-based receiver was also reported in other works [21, 35]. Moreover, we also measured the atomic response in case of constant  $f_{\text{OPT}} = 5 \text{ MHz}$  with changing frequencies of SIG and DRS fields, for which we observed drop to the noise level at the frequencies  $f_{\text{SIG}} \approx 2450 \text{ MHz}$  and  $f_{\text{SIG}} \approx 2550 \text{ MHz}$ .

As it can be noted on figs depicting comparisons between numerical predictions and measured data, the fit is not perfect and significant deviations can be observed. As mentioned earlier, such behavior is expected and can be attributed to splitting of the degeneracy of the Rydberg state due to the strong MW fields. To resolve such problem, it was already shown, that one can split the degenerate structure by applying the magnetic field and introduce the Zeeman shift to atomic ensemble [36]. Additionally, similar effect could be achieved by introducing the AC-Stark shifts. Moreover, both of methods of better resolving the energy structure of Rydberg states could help better match theoretical predictions with the measurements and, in effect, allow for better understanding of closed loop scheme dynamics.

**Funding.** Narodowe Centrum Nauki (2021/41/N/ST2/03114); European Funds for Smart Economy (FENG.02.01-IP.05-0017/23); Foundation for Polish Science;



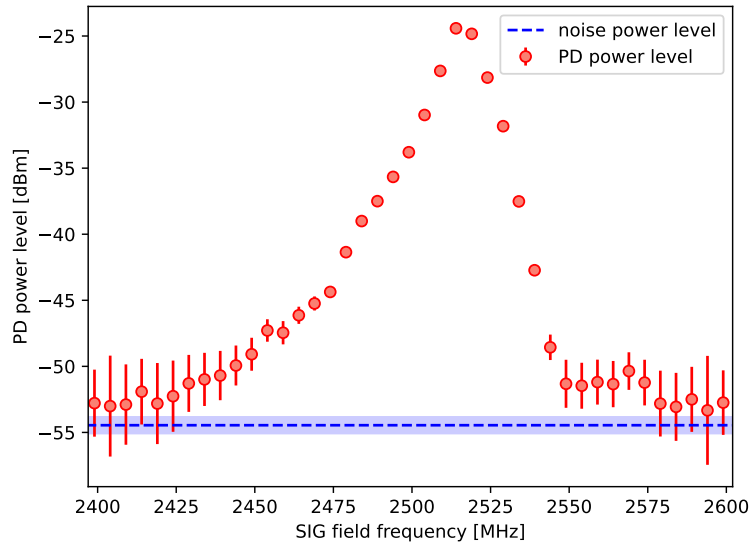


Fig. 6. Atomic response power level as a function of the SIG field frequency together with the shot-noise power level. The atomic response was measured for different frequencies of the SIG and DRS fields with a value of  $f_{\text{OPT}}$  being fixed and equal to  $f_{\text{OPT}} = 5$  MHz. The blue area around the shot-noise power level corresponds to the standard error of the calculated value.

**Acknowledgments.** This research was funded in whole or in part by National Science Centre, Poland grant No. 2021/41/N/ST2/03114. The „Quantum Optical Technologies” (FENG.02.01-IP.05-0017/23) project is carried out within the Measure 2.1 International Research Agendas programme of the Foundation for Polish Science co-financed by the European Union under the European Funds for Smart Economy 2021-2027 (FENG). We thank B. Kasza and S. Borówka for support and discussions.

**Disclosures.** The authors declare no conflicts of interest.

**Data availability.** Data has been deposited at Harvard Dataverse [37].

## References

1. C. T. Fancher, D. R. Scherer, M. C. S. John, and B. L. S. Marlow, “Rydberg atom electric field sensors for communications and sensing,” *IEEE Trans. on Quantum Eng.* **2**, 1–13 (2021).
2. G. Santamaria-Botello, S. Verploegh, E. Bottomley, and Z. Popovic, “Comparison of noise temperature of rydberg-atom and electronic microwave receivers,” (2022).
3. D. H. Meyer, P. D. Kunz, and K. C. Cox, “Waveguide-Coupled Rydberg Spectrum Analyzer from 0 to 20 GHz,” *Phys. Rev. Appl.* **15**, 014053 (2021).
4. Y. Cui, F.-D. Jia, J.-H. Hao, *et al.*, “Extending bandwidth sensitivity of Rydberg-atom-based microwave electrometry using an auxiliary microwave field,” *Phys. Rev. A* **107**, 043102 (2023).
5. M. T. Simons, J. A. Gordon, and C. L. Holloway, “Fiber-coupled vapor cell for a portable rydberg atom-based radio frequency electric field sensor,” *Appl. Opt.* **57**, 6456 (2018).
6. R. Mao, Y. Lin, K. Yang, *et al.*, “A high-efficiency fiber-coupled rydberg-atom integrated probe and its imaging applications,” *IEEE Antennas Wirel. Propag. Lett.* **22**, 352–356 (2023).
7. R. Zhao, M. Feng, J. Zhu, *et al.*, “Toward the measurement of microwave electric field using cesium vapor mems cell,” *IEEE Electron Device Lett.* **44**, 2031–2034 (2023).

8. J. A. Sedlacek, A. Schwettmann, H. Kübler, *et al.*, “Microwave electrometry with Rydberg atoms in a vapour cell using bright atomic resonances,” *Nat. Phys.* **8**, 819–824 (2012).
9. A. Osterwalder and F. Merkt, “Using High Rydberg States as Electric Field Sensors,” *Phys. Rev. Lett.* **82**, 1831–1834 (1999).
10. S. Borówka, U. Pylypenko, M. Mazelanik, and M. Parniak, “Sensitivity of a Rydberg-atom receiver to frequency and amplitude modulation of microwaves,” *Appl. Opt.* **61**, 8806–8812 (2022).
11. X. Liu, F. Jia, H. Zhang, *et al.*, “Using amplitude modulation of the microwave field to improve the sensitivity of rydberg-atom based microwave electrometry,” *AIP Adv.* **11**, 085127 (2021).
12. M. T. Simons, A. H. Haddab, J. A. Gordon, and C. L. Holloway, “A Rydberg atom-based mixer: Measuring the phase of a radio frequency wave,” *Appl. Phys. Lett.* **114**, 114101 (2019).
13. J. A. Gordon, M. T. Simons, A. H. Haddab, and C. L. Holloway, “Weak electric-field detection with sub-1 Hz resolution at radio frequencies using a Rydberg atom-based mixer,” *AIP Adv.* **9**, 045030 (2019).
14. M. Jing, Y. Hu, J. Ma, *et al.*, “Atomic superheterodyne receiver based on microwave-dressed rydberg spectroscopy,” *Nat. Phys.* **16**, 911–915 (2020).
15. S. Borówka, U. Pylypenko, M. Mazelanik, and M. Parniak, “Continuous wideband microwave-to-optical converter based on room-temperature Rydberg atoms,” *Nat. Photonics* **18**, 32–38 (2024).
16. J. Han, T. Vogt, C. Gross, *et al.*, “Coherent microwave-to-optical conversion via six-wave mixing in rydberg atoms,” *Phys. Rev. Lett.* **120**, 093201 (2018).
17. T. Vogt, C. Gross, J. Han, *et al.*, “Efficient microwave-to-optical conversion using rydberg atoms,” *Phys. Rev. A* **99**, 023832 (2019).
18. A. K. Robinson, N. Prajapati, D. Senic, *et al.*, “Determining the angle-of-arrival of a radio-frequency source with a Rydberg atom-based sensor,” *Appl. Phys. Lett.* **118**, 114001 (2021).
19. J. A. Sedlacek, A. Schwettmann, H. Kübler, and J. P. Shaffer, “Atom-Based Vector Microwave Electrometry Using Rubidium Rydberg Atoms in a Vapor Cell,” *Phys. Rev. Lett.* **111**, 063001 (2013).
20. D. A. Anderson, E. G. Paradis, and G. Raithele, “A vapor-cell atomic sensor for radio-frequency field detection using a polarization-selective field enhancement resonator,” *Appl. Phys. Lett.* **113**, 073501 (2018).
21. D. H. Meyer, K. C. Cox, F. K. Fatemi, and P. D. Kunz, “Digital communication with Rydberg atoms and amplitude-modulated microwave fields,” *Appl. Phys. Lett.* **112**, 211108 (2018).
22. Z. Song, H. Liu, X. Liu, *et al.*, “Rydberg-atom-based digital communication using a continuously tunable radio-frequency carrier,” *Opt. Express* **27**, 8848 (2019).
23. G. Morigi, S. Franke-Arnold, and G.-L. Oppo, “Phase-dependent interaction in a four-level atomic configuration,” *Phys. Rev. A* **66**, 053409 (2002).
24. D. V. Kosachiov, B. G. Matisov, and Y. V. Rozhdetsvensky, “Coherent phenomena in multilevel systems with closed interaction contour,” *J. Phys. B: At. Mol. Opt. Phys.* **25**, 2473 (1992).
25. S. Buckle, S. Barnett, P. Knight, *et al.*, “Atomic Interferometers,” *Opt. Acta: Int. J. Opt.* **33**, 1129–1140 (1986).
26. S. Berweger, A. B. Artusio-Glimpse, A. P. Rotunno, *et al.*, “Closed-loop quantum interferometry for phase-resolved Rydberg-atom field sensing,” *Phys. Rev. Appl.* **20**, 054009 (2023).
27. S. Borówka, M. Mazelanik, W. Wasilewski, and M. Parniak, “Optically-biased Rydberg microwave receiver enabled by hybrid nonlinear interferometry,” *Tech. rep.* (2024). ArXiv:2403.05310 [physics, physics:quant-ph] type: article.
28. D. Anderson, R. Sapiro, L. Gonçalves, *et al.*, “Optical Radio-Frequency Phase Measurement With an Internal-State Rydberg Atom Interferometer,” *Phys. Rev. Appl.* **17**, 044020 (2022).
29. D. Shylla, E. O. Nyakang’o, and K. Pandey, “Highly sensitive atomic based MW interferometry,” *Sci. Reports* **8**, 8692 (2018).
30. M. Fleischhauer, A. Imamoglu, and J. P. Marangos, “Electromagnetically induced transparency: Optics in coherent media,” *Rev. Mod. Phys.* **77**, 633–673 (2005).
31. C. Carr, M. Tanasittikosol, A. Sargsyan, *et al.*, “Three-photon electromagnetically induced transparency using rydberg states,” *Opt. Lett.* **37**, 3858–3860 (2012).
32. B. Kasza, S. Borówka, W. Wasilewski, and M. Parniak, “Atomic-optical interferometry in fractured loops: a general solution for rydberg radio frequency receivers,” (2024).
33. J. Nowosielski, M. Jastrzębski, P. Halavach, *et al.*, “Warm Rydberg atom-based quadrature amplitude-modulated receiver,” *Opt. Express* **32**, 30027–30039 (2024).
34. E. J. Robertson, N. Šibalić, R. M. Potvliege, and M. P. A. Jones, “ARC 3.0: An expanded Python toolbox for atomic physics calculations,” *Comput. Phys. Commun.* **261**, 107814 (2021).
35. C. L. Holloway, M. T. Simons, J. A. Gordon, and D. Novotny, “Detecting and Receiving Phase-Modulated Signals With a Rydberg Atom-Based Receiver,” *IEEE Antennas Wirel. Propag. Lett.* **18**, 1853–1857 (2019).
36. N. Schlossberger, A. P. Rotunno, A. B. Artusio-Glimpse, *et al.*, “Zeeman-resolved autler-townes splitting in rydberg atoms with tunable resonances and a single transition dipole moment,” *Phys. Rev. A* **109**, L021702 (2024).
37. J. Nowosielski, M. Mazelanik, W. Wasilewski, and M. Parniak, “Replication Data for: Superheterodyne Rydberg S-band receiver with a multi-tone local oscillator based on an atomic transition loop,” Type: dataset.